Electronic transport and spin-polarization effects of relativisticlike particles in mesoscopic graphene structures

V. Nam Do, V. Hung Nguyen, P. Dollfus, and A. Bournel

Citation: Journal of Applied Physics **104**, 063708 (2008); doi: 10.1063/1.2980045
View online: http://dx.doi.org/10.1063/1.2980045
View Table of Contents: http://scitation.aip.org/content/aip/journal/jap/104/6?ver=pdfcov
Published by the AIP Publishing

Electronic transport and spin-polarization effects of relativisticlike particles in mesoscopic graphene structures

V. Nam Do,[1,2,a)] V. Hung Nguyen,[1,3] P. Dollfus,[1] and A. Bournel[1]
[1]*Institut d'Electronique Fondamentale, UMR8622, CNRS, Universite Paris-Sud, 91405 Orsay, France*
[2]*Hanoi Advanced School of Science and Technology, 1 Dai Co Viet Str., Hanoi 10000, Vietnam*
[3]*Theoretical Department, Institute of Physics, VAST, P.O. Box 429, Bo Ho, Hanoi 10000, Vietnam*

(Received 25 March 2008; accepted 21 July 2008; published online 23 September 2008)

Motivated by recent studies on the use of graphene for new concepts of electronic/spintronic devices, the authors develop an efficient calculation method based on the nonequilibrium Green's function to solve the quantum relativisticlike Dirac's equation that governs the low-energy excited states in graphene. The approach is then applied to investigate the electronic transport and the spin polarization in a single-graphene barrier structure. The obtained results are presented and analyzed in detail aiming to highlight typical properties of the considered graphene structure as well as the efficiency of the developed approach that both may be helpful for further development in electronic devices and in spintronics. © *2008 American Institute of Physics*. [DOI: 10.1063/1.2980045]

I. INTRODUCTION

While strictly two-dimensional (2D) systems were not expected to exist, the experimental discovery of monolayer graphene sheets and other 2D atomic crystallites[1,2] has been a breakthrough and graphene rapidly became the subject of intensive experimental and theoretical researches in material science, condensed matter physics,[3] and even device applications.[4] It is basically due to the very specific conical shape of the electronic structure at the six edge corner points (often named the Dirac points or *K*-points) of the hexagonal Brillouin zone. It results in the so-called charge-conjugation symmetry between electron and hole states, which gives to the resulting massless particles a relativisticlike behavior. Experimentally, a lot of peculiar phenomena such as the finite value of the conductance at zero concentration and the unusual half-integer quantum Hall effect[5] has been observed in graphene and theoretically described in the frame of the massless fermion Dirac's model.[2,6]

Considering these properties, the transport of charges in various graphene-based structures such as the single and multibarrier,[7–11] quantum wells,[12] as well as *p-n* junctions[13] has been recently discussed. At the theoretical level, such studies are usually based on the nonequilibrium Green's function (NEGF) method to treat a tight-binding model of the original graphene honeycomb lattice,[14–16] or on the scattering matrix approach, i.e., by matching scattering states at the device interfaces, to study Dirac's equation.[7,10–12] However, both methods have certain limitations for practical use, e.g., the former one is generally of high computational cost and the latter is not suitable for further development, in particular, to take into account effects of defects, impurities,[17] spin-orbit coupling,[18] etc. Actually, the NEGF method is general and in the field of device simulation, it has been proven to be very efficient to study the quantum transport of charges in various ordinary semiconductor-based device structures (see Ref. 19 and references therein). The advantage of the method lies in the fact that it is very flexible to use for solving either atomistic tight-binding models or the ones based on the effective mass approximation. In this paper we present a development of the NEGF method to solve directly Dirac's equation, i.e., an effective model to describe low-energy particles in graphene. Compared to the atomistic tight-binding NEGF method, our approach is very efficient and particularly less computationally expensive. Based on that, we are able to systematically investigate the transport properties of different graphene-based structures. However, in the current work, we focus on electronic transport properties and spin-polarization effects of charges in the single-barrier structure which, although simple, characterizes some typical features of transport in graphene. The aim of this paper is not only to prove the efficiency of the developed method but also to highlight a general picture of the charge transport in graphene-based structures that may be helpful for the development of carbon-based technology.

The paper is thus organized as follows. First of all in Sec. II, we reformulate the NEGF method to solve Dirac's equation. Although effects of lattice defects and impurities are not taken into account, the problem is not trivial because one needs to solve 2×2 self-energy matrices that describe the coupling between the device and the contacts. A detailed analytical solution to this problem is presented. The formalism is then applied to explore and analyze general transport properties of charges in the considered structure. The transmission coefficient is determined through Green's functions and then used to calculate the conductance and the current using the Landauer formula. Numerical results and discussions are presented in Sec. III. Finally, Sec. IV is for the conclusion.

II. MODEL AND FORMULATION

We now generally consider a model of graphene under zero external magnetic field. The excited states around the Dirac points are thus described by the equation[6,9]

[a)]Electronic mail: vannam.do@gmail.com.

$$H = v_F(\sigma_x p_x + \sigma_y p_y) + U\sigma_0, \tag{1}$$

where σ_x, σ_y (and σ_z) are the Pauli matrices, which are used to describe the so-called pseudospin (not real spin) of particles, and σ_0 is the 2×2 identity one. The term $U\sigma_0$ is added to describe the charges under an electrostatic potential U, which can be practically created by the electric field effect of a gated insulator thin film[1,2,5,20] or by local chemical doping.[21–23] We additionally assume that the emitter and collector graphene sheets are semi-infinite and large enough for U to be just considered as a function of x. In Eq. (1) the quantity v_F is the Fermi velocity which, in the graphene case, is used instead of the light speed c in the original form of Dirac's equation.

According to the above assumptions, it is numerically convenient to represent the Hamiltonian [Eq. (1)] in the basis $\{|x_i\rangle \otimes |k_y\rangle\}$, where k_y denotes the wave vector along the OY direction and $a=x_{i+1}-x_i$ is the mesh spacing ($i\leq 0$ for the left contact, $i\in[1,N]$ for the device active region, and $i \geq N+1$ for the right contact). For simplicity we henceforth use the energy unit of $E_0=\hbar v_F/2ae$ (e denotes the absolute electron charge). The tight-binding representation of the Hamiltonian [Eq. (1)] in the real space is therefore written as

$$H_{i,i'} = i\sigma_x\delta_{i-1,i'} + (E_y\sigma_y + U_i\sigma_0)\delta_{i,i'} - i\sigma_x\delta_{i+1,i'}, \tag{2}$$

where $E_y=2ak_y$ and U are dimensionless and δ_{ij} is the Kronecker symbol. The onsite and coupling Hamiltonian matrices read $H_{ii}=E_y\sigma_y+U_i\sigma_0$, $T_{i,i-1}=i\sigma_x$, and $T_{i,i+1}=-i\sigma_x$, respectively.

In Green's function language the problem of device-contact coupling is systematically solved as a boundary condition, which is encoded in terms of the so-called self-energy. Within the model described by Eq. (1) the transport is considered to be ballistic and solving a set of nonequilibrium Green's functions reduces to solve only one of them, e.g., the retarded function $G^r(E)$ that is formally defined as

$$G^r(E) = [E + i0^+ - H - \Sigma_L^r(E) - \Sigma_R^r(E)]^{-1}, \tag{3}$$

where $\Sigma^r_{L(R)}(E)$ are the device-(L/R) contact coupling self-energies. According to Ref. 19, the calculation of $\Sigma^r_{L(R)}$ that just requires to find the contact surface retarded Green's function $G_0^r(E)$ since, e.g., $\Sigma_L^r(E)=T_{10}G_0^r(E)T_{01}=\sigma_x G_0^r(E)\sigma_x$, i.e., in terms of $X=-i\sigma_x G_0^r$ one has to solve the equation

$$X^2 - \alpha X + \beta = 0, \tag{4}$$

where $\alpha=T_{-10}[T_{-10}(E-H_{00}+i0^+)^{-1}T_{0-1}]^{-1}=E_y\sigma_z-i(E-U_0)\sigma_x$ and $\beta=T_{-10}[T_{0-1}]^{-1}=-\sigma_0$.

To solve Eq. (4) we distinguish some specific cases. The first one is the case where α is equal to zero, i.e., $E_y=0$ and $E-U_0=0$. In this case the solution of Eq. (4) is not unique. For simplicity we can choose $X=\sigma_z$ so that $\Sigma_L^r(E)=-\sigma_y$. The second case is $E_y\neq 0$ but $E=U_0$. Accordingly, α is diagonal and thus the matrix equation [Eq. (4)] simply reduces to two independent quadratic ones. Straightforwardly, we obtain the result $\Sigma_L^r=-X_0\sigma_y$, where

$$X_0 = E_y/2 - \mathrm{sgn}(E_y)\sqrt{1+(E_y/2)^2} \tag{5}$$

is a real number.

We now consider the case where $E-U_0\neq 0$. Solving the general 2×2 matrix equation [Eq. (4)] is not trivial but it also can be transformed into two independent quadratic equations in the eigenvalue representation of the matrix α since β is simply proportional to σ_0. For the sake of convenient physical interpretation we formally express the two eigenvalues of α in the form $\lambda_\pm=\pm iE_x$ where the quantity

$$E_x = \sqrt{(E-U_0)^2 - E_y^2} \tag{6}$$

can be real or imaginary and will be interpreted later. To go further in the calculation we assume that E_x is a real number. We therefore specify the form of the two matrices $D=(\sigma_0 - \gamma\sigma_y)/\sqrt{2}$, where $\gamma=(E_y-iE_x)/(E-U_0)$ and its inversion $D^{-1}=\sqrt{2}(\sigma_0+\gamma\sigma_y)/(1-\gamma^2)$, which are used to diagonalize α or to return results from the eigenvalue representation into the original one.

Now, multiplying Eq. (4) on the left and on the right side by D^{-1} and D, respectively, the matrix X is diagonalized and becomes $\bar{X}=iX_0\sigma_z$, where the factor X_0 is chosen as

$$X_0 = E_x/2 - i\ \mathrm{sgn}(E-U_0)\sqrt{1-(E_x/2)^2}. \tag{7}$$

In this case, X_0 is a complex number wherein the sgn-function is added to ensure results to be finite and to correspond to the retarded functions.[19] After some simple algebra we get the expression

$$\Sigma_L^r(E) = \frac{X_0}{E_x}\begin{pmatrix} E-U_0 & iE_y \\ -iE_y & E-U_0 \end{pmatrix}. \tag{8}$$

This equation is also applied when E_x, and thus X_0, is a pure imaginary number. However, only the case where E_x is a no null real number that corresponds to a transport state of charges. In this case, E_x is interpreted as the incident energy of particles injected from the contact into the device active region, or vice versa. Similarly, the expression of $\Sigma_R^r(E)$ is simply obtained by replacing U_0 in the above equation by U_{N+1}. Additionally, it is interesting to note that the above calculations can be straightforwardly developed for the massive fermion Dirac's case, i.e., adding the mass term $mv_F^2\sigma_z$ into Eq. (1). By setting $\gamma_1=(E_y-iE_x)/(E-U_0-imv_F^2)$ and $\gamma_2=(E_y-iE_x)/(E-U_0+imv_F^2)$, Eq. (8) is generalized to

$$\Sigma_L^r(E) = \frac{X_0}{1-\gamma_1\gamma_2}\begin{pmatrix} 2i\gamma_2 & -(1+\gamma_1\gamma_2) \\ (1+\gamma_1\gamma_2) & 2i\gamma_1 \end{pmatrix}. \tag{9}$$

Our formalism may also be applied to the case of low-energy excited states in bilayer grapheme, but much more attention should be made on Eq. (4) since β is no longer simply proportional to σ_0.

Using Eqs. (2) and (8) Green's function $G^r(E)$ [Eq. (3)] is straightforwardly determined and then transport properties of the structure can be extracted. Considering that we are interested in the case of electrons injected from the leads, the transmission coefficient, which is needed to calculate the current using Landauer's formula,[10,24] can be determined as

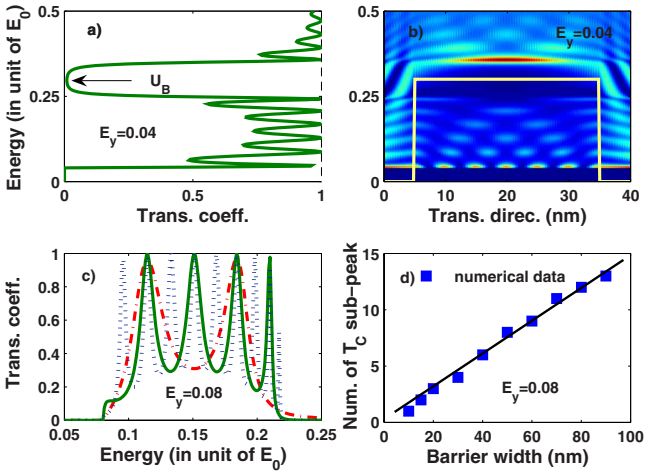

FIG. 1. (Color online) (a) Transmission coefficient T of the unbiased single-barrier structure as a function of energy E. (b) Local density of states plotted for $E_y=0.04$ clearly showing the formation of the hole states inside the potential barrier and the valley around U_B. The white solid line is plotted for the eye guide of the potential profile. (c) The dependence of T_C on the different barrier widths, $W=15$ (dot dashed line), 30 (solid line), and $W=60$ nm (dashed line). (d) The linear dependence of the subpeak number of T_C on the barrier width. The barrier height $U_B=0.3$. All energies are given in the unit of $E_0=\hbar v_F/2ae$ (≈ 1.65 eV).

$$T(E,E_y)=\sum_{i,j=1}^{2}\Gamma^L_{1,i}G^r_{i,2N-1}\Gamma^R_{1,j}G^a_{2N-2+j,1}, \tag{10}$$

where $\Gamma^{L(R)}=i[\Sigma^r_{L(R)}-\Sigma^a_{L(R)}]$ are the tunneling rates and the advanced functions $G^a=[G^r]^\dagger$ and $\Sigma^a=[\Sigma^r]^\dagger$.

III. APPLICATION AND DISCUSSIONS

A. General features of charge transport

We now apply this formalism to investigate transport properties of charges in a rectangular single-graphene barrier structure (as described in Ref. 9). Although simple, this typical structure may highlight fundamental microscopic pictures of charges in graphene, e.g., the charge-conjugation symmetry, the chirality, etc.[9] Additionally, it can give rise to interesting behaviors of the *I-V* characteristics, e.g., the negative differential conductance (NDC).[7,24] Throughout the work, the mesh spacing a and the temperature are chosen to be 0.2 nm and 0 K, respectively. In Fig. 1(a) we display the transmission coefficient T for a structure of barrier width (W) and height (U_B) of 30 nm and 0.3, respectively, in the positive energy branch and with different values of E_y to highlight the chiral property of transport. At finite values of E_y the transmission coefficient exhibits an energy valley of width $2E_y$, centered on the U_B value, whose depth depends on W and E_y. This valley separates the transmission coefficient into two parts, called here T_C and T_N, corresponding to the energy ranges (E_y, U_B-E_y) and $(U_B+E_y,+\infty)$, respectively. The most important feature in Fig. 1(a) is that, in contrast to the case of ordinary semiconductors, the transmission coefficient does not exponentially decay in the energy range below U_B but exhibits oscillations with resonantlike subpeaks reaching the value of 1. Indeed, the appearance of such peaks is essentially due to the resonance or the good matching of electron states and hole states outside/inside the barrier region, respectively. It is clearly shown in Fig. 1(b) where we plot the map of the local density of states (LDOS) for $E_y=0.04$. Both the energy valley around U_B and the available states in the valence band of the barrier appear. Accordingly, electrons do not transfer through the barrier but they transform themselves to holes, then do again to electrons when entering and leaving the barrier, respectively. Such a transport process is essentially a consequence of the charge-conjugation symmetry described by Dirac's model, wherein a particle and its antiparticle can be interchangeably transformed to each other. For $E_y=0$ the transmission coefficient is equal to 1. This fact is nothing, but the manifestation of the so-called Klein's paradox, which states that the potential barrier is transparent for zero-angle incident relativistic particles whatever the barrier height and width, is well known in quantum electrodynamics and is expected to be experimentally verified in such a graphene structure.[9]

We proceed to analyze in more details the formation of hole states inside the barrier region from the behavior of T_C. Basically, the positions of subpeaks of T_C inform about the energy structure of hole bound states inside the barrier region. The number of subpeaks generally depends on the barrier height and width [see Fig. 1(c)], but it depends also on the incident direction of particles [Fig. 1(a)]. In Ref. 12 the picture of the confinement of electron states in a graphene-based quantum well was investigated. The authors concluded that the motion of particles along the well can suppress Klein's tunneling and thus generate the confinement of electrons. This picture is directly applied to our situation because the barrier is actually a well for holes. Our numerical data are in agreement with that conclusion. For instance, when increasing E_y the width of T_C, and thereby the number N of subpeaks, is reduced. Particularly, the positions of T_C subpeaks are well fitted by the expression[12] $|E-U_B|=\sqrt{(2a\pi n/W)^2+E_y^2}$ for E_y that is large enough, for instance, when $E_y>0.08$. Although we do not show the result of this fit, we would like to verify another consequence of this formula. Indeed, according to it, the ratio of the number N of T_C subpeaks to the barrier width should be a constant. In our calculation this point is confirmed and illustrated in Fig. 1(d) by the linear dependence of N on W. This result therefore implies an unusual quantization of quasirelativistic hole states in the barrier region that is definitely different from the case of normal holes wherein $|E-U_B|\propto n/W^2+\hbar^2k_y^2/2m^*$.

Such features of hole states of course govern the behavior of observables, e.g., the conductance G, as illustrated in Fig. 2 wherein we plot the dependence of G on the Fermi energy E_F for different values of the barrier height (left) and width (right). Generally speaking, when increasing E_F the conductance rises up to a maximum at $E_F=U_B/2$ and then goes down to a minimum when $E_F=U_B$.[10] Although E_y is already integrated, G exhibits clearly subpeaks in the range of $(0,U_B/2)$ showing the importance of the hole state quantization. From the numerical data we also realize that the conductance depends strongly on U_B [Fig. 2(a)] but weakly on W. Indeed, in the latter case the curves plotted in Fig. 2(b) for $W=15$ (dashed line), 30 (solid line), and 60 nm (dot dashed line) only differ in the minimum value $G_{\min}$ at $E_F=U_B=0.3$. It is also very interesting to note that for particular

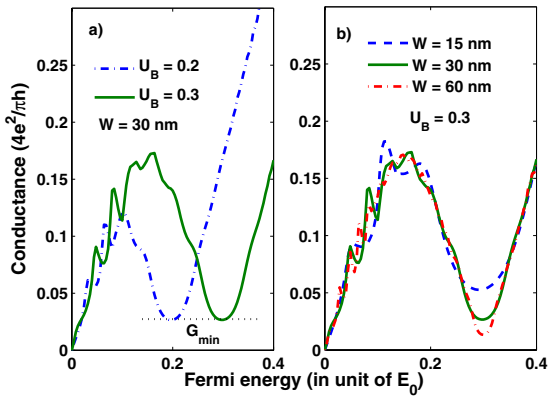

FIG. 2. (Color online) Conductance as a function of Fermi energy plotted for different values of barrier (a) height and (b) width.

values of W, the minimum conductance $G_{\min}$ seems to be a constant independent of U_B. Roughly speaking, it could be understood using the picture of Klein's paradox. As already shown in Fig. 1(a) the transmission coefficient $T(E)$ exhibits a valley around U_B for finite E_y, the transport properties of charges, and therefore $G_{\min}$, are thus ruled out by particles arriving at the barrier surface with a small incident angle (depending on W) for which the barrier is almost transparent. Actually, this comment is just correct for U_B not so small that hole confined states are formed in the barrier region. In the critical limit $E_F=U_B=0$, i.e., when the electron and hole states are degenerate, $G_{\min}$ is null. This seems to be in contrast with the experimental observations of a finite minimum value of the conductivity $\sigma_{\min}$ in the neutral case $E_F=U_B=0$. However, it should be said that the common theoretical value $\sigma_{\min}=4e^2/\pi h$ when $E_F=U_B=0$ can be reproduced in our calculation by just imposing a high value of the contact electrostatic potentials U_0 and U_{N+1} as in Refs. 25 and 26 (remembering that here the graphene emitter/collector is modeled by assuming $U_0=U_{N+1}=0$).

Now we go to explore the current-voltage (I-V) characteristics of the structure. To do so we additionally plot in Fig. 3 the LDOS (left) and the transmission coefficient (right) for the case of finite bias (concretely, $V=0.3$ and $E_y=0.04$). The

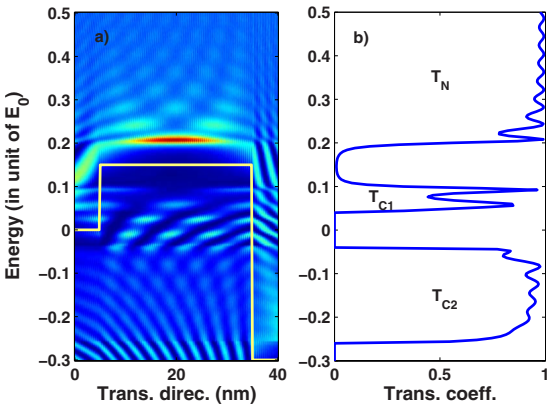

FIG. 3. (Color online) (a) LDOS and (b) transmission coefficient plotted for finite bias ($V=0.3$) showing the electron and hole states above and below the electrostatic potential profile, which therefore leads to the appearance of the three separate transport domains, T_N, T_{C1}, and T_{C2}. Other parameters are $E_y=0.04$ and $U_B^0=0.3$.

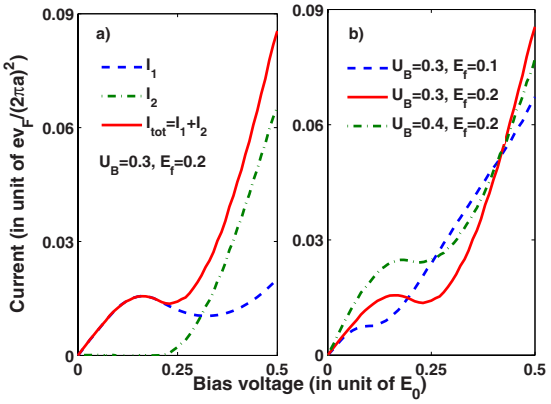

FIG. 4. (Color online) Current-voltage characteristics [in unit of $ev_F/(2\pi a)^2$ ($\approx 10^5$ A/m)]: (a) the form of the two current components I_1 and I_2 as well as of the total one I_{tot}; and (b) the total current for different values of U_B and U_F.

figure reveals that besides T_N and T_{C1} in the positive energy range, another non-null part, namely, T_{C2}, of the transmission coefficient appears in the negative energy range of $(-V+|E_y|,-|E_y|)$ when applying a bias voltage V (here V is also measured in unit of E_0). Accordingly, T_{C2} can importantly contribute to the total current when the bias is high enough. For this reason we denote I_1 the current governed by T_N and T_{C1}, and I_2 the contribution related to T_{C2}. The total picture of the transport can be depicted as follows: at high energy ($E>U_B$) the transport is simply the passage of electrons from one electrode to the another; in the energy range $(0,U_B)$, it is a process of successive transformation between the electron and hole states or the chiral tunneling; and in the negative range $(-V,0)$ the transport can be seen as the band-to-band transmission, i.e., from the valence band to the conduction one, or the interband tunneling. When rising the bias, the width of T_{C2} is simply enhanced, the current I_2 therefore monotonically increases, while the current I_1 can rapidly get the saturation if the potential barrier height is frozenly fixed. However, both T_N and T_{C1} can be shifted by changing the value of U_B (see Fig. 1). We therefore assume the dependence of U_B on the bias voltage V similarly to that in Ref. 7, i.e., $U_B=U_B^0-V/2$, where U_B^0 is the initial value for $V=0$. Consequently, when increasing the bias, T_N is shifted downward in the energy range, and the width of T_{C1} is shrunk while that of T_{C2} is broadened. That evolution of the transmission coefficient versus the bias therefore may induce interesting features of the current-voltage characteristic.

Indeed, we plot in Fig. 4(a) the total current (solid line) and its two components I_1 (dashed line) and I_2 (dot dashed line) as a function of bias. From the figure, we observe different behaviors of I_1 and I_2. Concretely, at low bias, $V<E_F$, while $I_2=0$, I_1 increases to a particular value (I_P) and then decreases to a lower one (I_V), which induces an effect of NDC.[7] If continuing rising the bias, I_1 can then increase and get the saturation when $U_B=0$, i.e., when T_{C1} totally disappears and T_N essentially governs the transport in the positive energy range. Here we limit the bias range from 0 to 0.5 (≈ 0.8 V) so the saturation is not shown. I_2 is turned on when $V=E_F$ and then rapidly increases versus the bias. Accordingly, the behavior of the total current is essentially gov-

erned by I_1 at low bias and by I_2 at high bias. Around the value $V=E_F$, the NDC behavior can be still observed on the total current but it is extremely weak. This is obviously in contrast with the results presented in Ref. 7 wherein the NDC is very significant with a very high value of the peak-to-valley ratio $\gamma=I_P/I_V$. However, in a recent comment, we pointed out the shortcoming in that article concerning the analysis of the *I-V* characteristic of the structure.[24] Basically, it is due to the neglect of the current component I_2. In our comment, we repeated the calculation of matching the wave functions at the barrier interface for each particular energy domain. Here, we used the NEGF approach presented above and achieved the good agreement between both. By changing different parameters, such as the width W and the height U_B^0 of the barrier as well as the contact Fermi level, we realize that the current is almost independent of W and that it is difficult to reach a high γ. Actually, the possible negative differential conductance originates from the shrinking of T_{C1} resulting from a bias voltage increase. So, if E_F is much smaller or larger than U_B, the contributions of T_{C2} and T_N to the current become the most important. This point is illustrated in Fig. 4(b) by the three curves, the dashed ($U_B=0.3, E_F=0.1$), the solid ($U_B=0.3, E_F=0.2$), and the dot dashed ($U_B=0.4, E_F=0.2$) lines. Additionally, it is interesting to notice from Fig. 4(b) that the latter curve ($U_B=0.4$) is higher than the second one ($U_B=0.3$) in the medium range of bias, but at high bias, this order is changed after a crossing of the two curves. Actually, this result can be elucidated through the form of I_1 since I_2 is totally independent of U_B^0 ($U_B^0 > E_F$). Basically, the value of I_1 is determined by the width of T_{C1}, which is larger if U_B^0 is higher, so that $I_1(U_B^0=0.4) > I_1(U_B^0=0.3)$. The large width of $T_{C1}(U_B^0=0.4)$ compared to that of $T_{C1}(U_B^0=0.3)$ also means that the minimum of $I_1(U_B^0=0.4)$ should be achieved at higher voltage than that of $I_1(U_B^0=0.3)$. Accordingly, these two curves cross each other at a high voltage because while $I_1(U_B^0=0.4)$ is decreasing, $I_1(U_B^0=0.3)$ rapidly rises up to get the saturation. This picture is also met in the following part of the study when we introduce magnetic effects into the barrier region of the considered structure.

B. Spin-polarization transport

Beside its interesting electronic transport properties, graphene nowadays is strongly expected to have applications in spintronics[27] because of the very weak spin-orbit interaction that leads to a long spin-flip length (≈ 1 μm).[28] In what follows, we will present results of spin-polarization transport in the considered structure by adding a Zeeman's term $-\sigma h$ (defined only in the barrier region) into Eq. (1), where $\sigma = \pm 1$ denotes the spin of particles and h the spin splitting energy. Practically, this term is caused by a magnetic moment in graphene that can be introduced intrinsically, e.g., by doping[29] and defects,[22,30] or extrinsically by a so-called proximity effect,[31] for instance. Our model is thus similar to that used in Refs. 31 and 32 but the calculation covers the whole range of bias voltage. Additionally, it should be well noticed that, in principle, to include the real spin degrees of freedom of electrons and holes, the results presented as the 2×2 matrices in Sec. I should be generalized into the 4×4 ones. However, since no spin-flip process is considered here, those results still hold for each kind of particles with their own spins. Generally speaking, spin splitting just shifts the conductance of each spin channel relatively to each other, leading to the appearance of the separation of the total conductance peak when rising up h as seen in Fig. 6 of Ref. 31. This separation, as proposed in Ref. 31, is the measurement of the intensity of the proximity exchange effect. In Fig. 5, we display the oscillation behavior of the conductance of each spin channel and the spin polarization $P=(G_\uparrow - G_\downarrow)/(G_\uparrow + G_\downarrow)$ as functions of the barrier height U_B [Figs. 5(a) and 5(b), respectively] as already reported in Ref. 32. Obviously, the oscillation of P is due to that of $G_\uparrow$ and $G_\downarrow$ and depends on the spin splitting energy h. If this quantity is extrinsically tuned by the so-called proximity effect, for example, the oscillations of P may be enhanced or suppressed according to the mixing of two coherent/decoherent phase waves. The oscillations of $G_{\uparrow,\downarrow}$ basically come from the good matching between the electron and hole states at the barrier interfaces. Indeed, this result appears clearly from the expression of the transmission coefficient for σ-particles in the limit of $U_B \gg E_F$,[9]

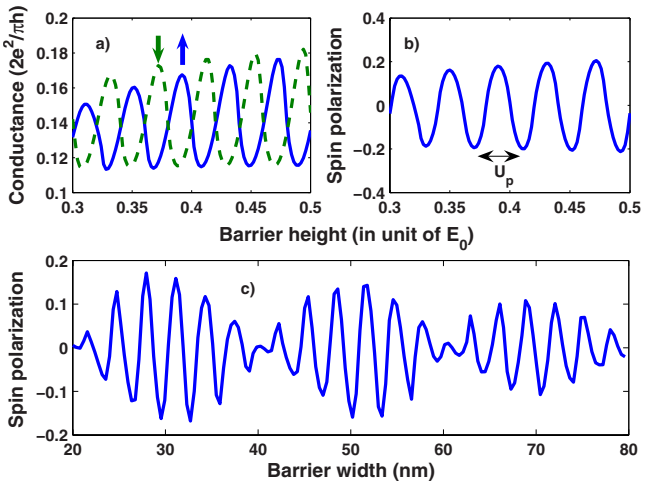

FIG. 5. (Color online) (a) Oscillations of the conductance G_σ and (b) the spin polarization P vs the barrier height U_B. As function of the barrier width W, (c) the oscillations of P are modulated into the beating picture, which is due to the different periods of $G_\uparrow$ and $G_\downarrow$. The Fermi level $E_F=0.2$, $U_B=0.5$, and $h=0.03$ are chosen to follow the condition $U_{B\sigma} \gg E_F$.

$$T_\sigma(\theta, U_B) = \frac{\cos^2\theta}{1-\cos^2(q_x^\sigma W)\sin^2\theta}, \tag{11}$$

where $q_x^\sigma = \sqrt{(E-U_{B\sigma})^2/\hbar^2 v_F^2 - k_y^2} \approx U_{B\sigma}/\hbar v_F$ and $U_{B\sigma}=U_B-\sigma h$. Accordingly, G_σ are oscillatory functions of $U_{B\sigma}W/\hbar v_F$ that have their maximum/minimum values when $q_x^\sigma W$ is equal to an integer/half-integer multiple of π, respectively. From Eq. (11) it is also straightforward to see that $P \propto \sin(2U_B W/\hbar v_F)\sin(2hW/\hbar v_F)$. So, the spin polarization is actually an oscillatory function of U_B or/and h. The spacing between the two nearest peaks of P is straightforwardly evaluated as $\pi\hbar v_F/W$, which in terms of dimensionless quantities in our analysis, reads $U_P=2\pi a/W$. For instance, $W=30$ nm and $a=0.2$ nm yield $U_P=0.042$, which is very

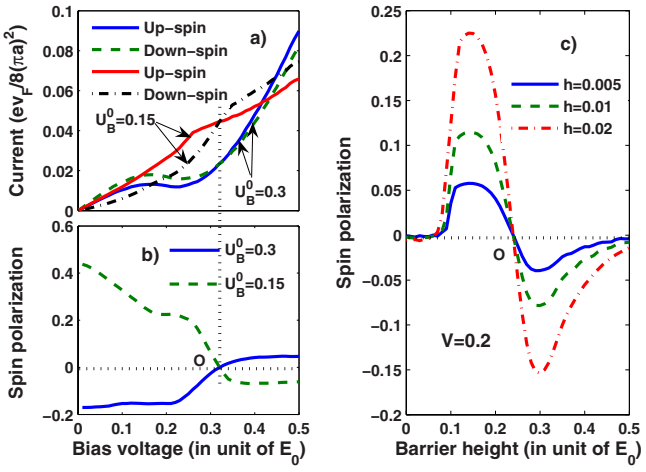

FIG. 6. (Color online) (a) The *I-V* curves of each spin channels and (b) the spin polarizations, plotted for the two cases of high and low barrier heights $U_B^0=0.3$ and $U_B^0=0.15$, $h=0.02$. (c) The spin polarization extracted at $V=0.2$ and various h as a function of the barrier height that can be tuned by gate voltage. The Fermi level is chosen as $E_F=0.2$.

close to our numerical result $U_P \approx 0.04$. It is also interesting to note that the spin polarization P is a modulated oscillatory function of the barrier width W. In Fig. 5(c) we display the dependence of the spin polarization P on W for $U_B=0.5$, $h=0.03$ and $E_F=0.2$ obtained from our calculation approach. The figure obviously shows the beating behavior of the oscillation of P, which is in good agreement with the above analysis.

For finite biases we are also interested in the behavior of the polarization of the spin current $P=(I_\uparrow - I_\downarrow)/(I_\uparrow + I_\downarrow)$. Since the barrier height of the considered structure can be tuned by the gate, we explore the variation in P on both V and U_B^0. In Fig. 6(a) we draw the currents of the two spin channels for $U_B^0=0.3$, the solid (spin-up) and the dashed (spin-down) lines, and for $U_B^0=0.15$, the red solid (spin-up) and the dot dashed (spin-down) lines. In both cases we see that the spin-up and the spin-down curves cross each other at points seemingly with the same bias, $V_O \approx 0.32$. However, if $I_\uparrow < I_\downarrow$ for the case of high barrier ($U_B^0 > E_F$) when $V < V_O$, and vice versa when $V > V_O$, this order can be changed in the case of low barrier ($U_B^0=0.15 < E_F$). This fact can be understood through the picture of the transmission coefficient. Basically, it is due to the role of T_{C1} on the transport. In the former case, it is totally similar to that seen in Fig. 4(b) for the solid and the dot dashed lines since the spin-down electrons see a higher potential barrier than that the spin-up electrons. In the case of low barrier U_B^0, the influence of T_{C1} decreases and the current is dominated by T_N. As a consequence, the lower the potential barrier, the higher the current. At high voltage, both T_N and T_{C2} are important, but since the contribution of T_N is unchanged and the effective width of T_{C2} for the spin-down channel is larger than that for the spin-up one (not shown), the form of the total current is essentially governed by T_{C2}. Accordingly, the picture of the polarization of the spin currents as a function of the bias voltage looks like the one shown in Fig. 6(b), wherein when $V \in (0, V_O)$, $P<0$ for $U_B^0=0.3$ and $P>0$ for $U_B^0=0.15$; the sign is changed when $V > V_O$. To complete, we extract and plot the spin polarization P as a function of the barrier height at $V=0.2$ for three values of the spin splitting energy and plot results in Fig. 6(c). The figure reveals the crossing of the three curves, the solid ($h=0.005$), the dashed ($h=0.01$), and the dot dashed ($h=0.02$) lines, at one point, namely, O and apparently separates two domains of U_B^0 wherein P is positive ($U_B^0 < 0.24$) and negative ($U_B^0 > 0.24$). This feature therefore may suggest the ability of switching the spin current using the gate voltage.

IV. CONCLUSION

We have developed a calculation method based on the NEGF approach to solve Dirac's equation that is used to describe low-energy excited states in graphene. We have presented in detail the analytical treatment of the device-contact coupling problem that plays a crucial role to deduce transport properties of considered systems as the device active region. The method was then applied to analyze transport properties of charges in a typical graphene structure with a single potential barrier. By analyzing the behavior of the transmission as well as the local density of states, which are directly determined in our approach, the formation of hole confined states in the barrier region is highlighted, giving a general scenario of the charge transport. We then have analyzed the dependence of the conductance on the Fermi energy, the barrier height, and the width. The difference of the transport picture between normal semiconductors and graphene therefore has been pointed out, especially in the current-voltage characteristics. Additionally, we are also interested in the picture of the spin polarization of the considered system by introducing a magnetism in the barrier region that can be externally tuned. Moreover, the picture of the spin current polarization has also been studied systematically using our approach as the dependence of this quantity on the bias and the gate voltage. Our study therefore may be meaningful for future development in electronic devices and spintronics based on graphene.

ACKNOWLEDGMENTS

One of the authors (V.H.N.) acknowledges Université Paris-Sud, Orsay, France for financial support. This work was partially supported by the European Community through the Network of Excellence NANOSIL.

[1] K. S. Novoselov, A. K. Geim, S. V. Morozov, D. Jiang, Y. Zhang, S. V. Dubonos, I. V. Grigorieva, and A. A. Firsov, Science **306**, 666 (2004).
[2] K. S. Novoselov, A. K. Geim, S. V. Morozov, D. Jiang, M. I. Katsnelson, I. V. Grigorieva, S. V. Dubonos, and A. A. Firsov, Nature (London) **438**, 197 (2005).
[3] A. K. Geim and K. S. Novoselov, Nat. Mater. **6**, 183 (2007).
[4] M. C. Lemme, T. J. Echtermeyer, M. Baus, and H. Kurz, IEEE Electron Device Lett. **28**, 282 (2007).
[5] Y. Zhang, Y. W. Tan, H. L. Stormer, and P. Kim, Nature (London) **438**, 201 (2005).
[6] D. P. DiVincenzo and E. J. Mele, Phys. Rev. B **29**, 1685 (1984).
[7] D. Dragoman and M. Dragoman, Appl. Phys. Lett. **90**, 143111 (2007).
[8] R. Zhu and Y. Guo, Appl. Phys. Lett. **91**, 252113 (2007).
[9] M. I. Katsnelson, K. S. Novoselov, and A. K. Geim, Nat. Phys. **2**, 620 (2006).
[10] J. M. Pereira, Jr., P. Vasilopoulos, and F. M. Peeters, Appl. Phys. Lett. **90**, 132122 (2007).
[11] C. X. Bai and X. D. Zhang, Phys. Rev. B **76**, 075430 (2007).

[12]J. M. Pereira, Jr., V. Mlinar, F. M. Peeters, and P. Vasilopoulos, Phys. Rev. B **74**, 045424 (2006).
[13]V. V. Cheianov and V. I. Falko, Phys. Rev. B **74**, 041403(R) (2006).
[14]G. Liang, N. Neophytou, M. S. Lundstrom, and D. E. Nikonov, J. Appl. Phys. **102**, 054307 (2007).
[15]K. Kazymyrenko and X. Waintal, Phys. Rev. B **77**, 115119 (2008).
[16]Y. B. Chen, Y. E. Xie, and X. H. Yan, J. Appl. Phys. **103**, 063711 (2008).
[17]N. M. R. Peres, F. Guinea, and A. H. Castro Neto, Phys. Rev. B **73**, 125411 (2006).
[18]K. H. Ding, G. Zhou, and Z. G. Zhu, J. Phys.: Condens. Matter **20**, 345228 (2008).
[19]V. Nam Do, "Modeling and simulation of quantum transport in semiconductor nanometer devices," Ph.D. thesis, Paris-Sud University, 2007.
[20]B. Huard, J. A. Sulpizio, N. Stander, K. Todd, B. Yang, and D. Goldhaber-Gordon, Phys. Rev. Lett. **98**, 236803 (2007).
[21]E. H. Hwang, S. Adam, and S. Das Sarma, Phys. Rev. B **76**, 195421 (2007).
[22]T. O. Wehling, K. S. Novoselov, S. V. Morozov, E. E. Vdovin, M. I. Katsnelson, A. K. Geim, and A. I. Lichtenstein, Nano Lett. **8**, 173 (2008).
[23]F. Schedin, A. K. Geim, S. V. Morozov, E. W. Hill, P. Blake, M. I. Katsnelson, and K. S. Novoselov, Nat. Mater. **6**, 652 (2007).
[24]V. Nam Do, Appl. Phys. Lett. **92**, 216101 (2008).
[25]M. I. Katsnelson, Eur. Phys. J. B **51**, 157 (2006).
[26]J. Tworzydlo, B. Trauzettel, M. Tiov, A. Rycerz, and C. W. J. Beenakker, Phys. Rev. Lett. **96**, 246802 (2006).
[27]Y. G. Semenov, K. W. Kim, and J. M. Zavada, Appl. Phys. Lett. **91**, 153105 (2007).
[28]D. Huertas-Hernando, F. Guinea, and A. Brataas, Phys. Rev. B **74**, 155426 (2006).
[29]N. M. R. Peres, F. Guinea, and A. H. C. Neto, Phys. Rev. B **72**, 174406 (2005).
[30]O. V. Yazyev and L. Helm, Phys. Rev. B **75**, 125408 (2007).
[31]H. Haugen, D. Huertas-Hernando, and A. Brataas, Phys. Rev. B **77**, 115406 (2008).
[32]T. Yokoyama, Phys. Rev. B **77**, 073413 (2008).